Downloaded from orbit.dtu.dk on: Nov 07, 2026

DTU Library

Mesoscale tissue properties and electric fields in brain stimulation: bridging the macroscopic and microscopic scales using layer-specific cortical conductivity

Wang, Boshuo; Worbs, Torge H.; Hussain, Minhaj A.; Aberra, Aman S.; Thielscher, Axel; Grill, Warren M.; Peterchev, Angel V.

Published in:
Journal of Neural Engineering

Link to article, DOI:
10.1088/1741-2552/ae6ff0

Publication date:
2026

Document Version
Publisher's PDF, also known as Version of record

Link back to DTU Orbit

Citation (APA):
Wang, B., Worbs, T. H., Hussain, M. A., Aberra, A. S., Thielscher, A., Grill, W. M., & Peterchev, A. V. (2026). Mesoscale tissue properties and electric fields in brain stimulation: bridging the macroscopic and microscopic scales using layer-specific cortical conductivity. *Journal of Neural Engineering*, *23*(3), Article 036026. https://doi.org/10.1088/1741-2552/ae6ff0

General rights
Copyright and moral rights for the publications made accessible in the public portal are retained by the authors and/or other copyright owners and it is a condition of accessing publications that users recognise and abide by the legal requirements associated with these rights.

- Users may download and print one copy of any publication from the public portal for the purpose of private study or research.
- You may not further distribute the material or use it for any profit-making activity or commercial gain
- You may freely distribute the URL identifying the publication in the public portal

If you believe that this document breaches copyright please contact us providing details, and we will remove access to the work immediately and investigate your claim.

Journal of Neural Engineering

PURPOSE-LED PUBLISHING™

PAPER • **OPEN ACCESS**

Mesoscale tissue properties and electric fields in brain stimulation: bridging the macroscopic and microscopic scales using layer-specific cortical conductivity

To cite this article: Boshuo Wang *et al* 2026 *J. Neural Eng.* **23** 036026

View the article online for updates and enhancements.

You may also like

- Computational neuroelectrophysiology and artificial intelligence for drug-resistant epilepsy: recent advances, current challenges, and future directions
Yalin Wang, Zibo Yan, Yuanchu Gong et al.
- But do we need high bandwidth? Applications and scaling challenges of invasive brain–computer interfaces
Luca M Meyer and Majid Zamani
- Vestibular peripheral function remains robust after two weeks of continuous ionic direct current stimulation
Celia Fernández Brillet, W Mitchel Thomas, Katherine N Mueller et al.

This content was downloaded from IP address 192.38.90.153 on 24/07/2026 at 12:37

Journal of Neural Engineering

Check for updates

OPEN ACCESS

RECEIVED
4 February 2026

REVISED
30 April 2026

ACCEPTED FOR PUBLICATION
19 May 2026

PUBLISHED
2 June 2026

Original content from this work may be used under the terms of the Creative Commons Attribution 4.0 licence.

Any further distribution of this work must maintain attribution to the author(s) and the title of the work, journal citation and DOI.

PAPER

Mesoscale tissue properties and electric fields in brain stimulation: bridging the macroscopic and microscopic scales using layer-specific cortical conductivity

Boshuo Wang[1], **Torge H Worbs**[2,3], **Minhaj A Hussain**[4], **Aman S Aberra**[5,6], **Axel Thielscher**[2,3], **Warren M Grill**[4,7,8,9] and **Angel V Peterchev**[1,4,7,8,*]

[1] Department of Psychiatry and Behavioral Sciences, Duke University, Durham, NC, United States of America
[2] Section for Magnetic Resonance, DTU Health Tech, Technical University of Denmark, Kgs Lyngby, Denmark
[3] Danish Research Centre for Magnetic Resonance, Department of Radiology and Nuclear Medicine, Copenhagen University Hospital Amager and Hvidovre, Copenhagen, Denmark
[4] Department of Biomedical Engineering, School of Engineering, Duke University, Durham, NC, United States of America
[5] Department of Biological Sciences, Dartmouth College, Hanover, NH, United States of America
[6] Department of Molecular and Systems Biology, Dartmouth College, Hanover, NH, United States of America
[7] Department of Electrical and Computer Engineering, School of Engineering, Duke University, Durham, NC, United States of America
[8] Department of Neurosurgery, School of Medicine, Duke University, Durham, NC, United States of America
[9] Department of Neurobiology, School of Medicine, Duke University, Durham, NC, United States of America
[*] Author to whom any correspondence should be addressed.

E-mail: angel.peterchev@duke.edu

Keywords: electric field, tissue conductivity, neural activation, computational model, mesoscale

Abstract

Objective. Accurate simulations of electric fields (E-fields) in neural stimulation depend on tissue conductivity representations that link underlying microscopic tissue structure with macroscopic assumptions. Mesoscale conductivity variations can produce meaningful changes in E-fields and neural activation thresholds but remain largely absent from standard macroscopic models. Conductivity variations within the cortex are expected given the differences in cell density and volume fraction across layers. We sought to estimate layer-specific conductivity within the cortex using computational models. *Approach.* We review recent efforts modeling microscopic and mesoscopic E-fields and outline approaches that bridge micro- and macroscales to derive consistent mesoscale conductivity distributions. Using simplified microscopic models, effective tissue conductivity was estimated as a function of volume fraction of extracellular space, and the conductivities of different cortical layers were interpolated based on experimental volume fraction. *Main results.* The effective tissue conductivities were monotonically decreasing convex functions of the cell volume fraction. They followed the theoretical power formulas only for small volume fractions (<20%) and deviated to higher values for larger volume fractions. With decreasing cell volume fraction, the conductivity of cortical layers increased with depth from layer 2 to 6. Due to the high relative sensitivity, the conductivity difference between layers was considerably larger than their variation in volume fraction, e.g. with layers 3 and 6 being 5% and 24% more conductive than layer 2, respectively, despite their volume fraction being only 1.3% and 5% lower than that of the latter. *Significance.* The review and analysis provide a foundation for accurate multiscale models of E-fields and neural stimulation. Overcoming technical limitations that microscale and macroscale methods face will allow validation to arrive at consistent conductivity distributions. Using layer-specific conductivity values within the cortex could improve the accuracy of estimations of thresholds and distributions of neural activation in E-field models of brain stimulation.

© 2026 The Author(s). Published by IOP Publishing Ltd

1. Introduction

Accurate modeling of the electric field (E-field) generated by brain stimulation is crucial for estimating the stimulation dose [1], understanding the neural response [2], and improving performance via computational optimization [3]. Conventional E-field simulations assume homogeneity of tissue electrical properties on the macroscopic scale that represents an average of the microscopic cellular composition [4]. Unlike previous microscopic E-field simulations restricted to only a few simplified cells [5], the most recent models captured much larger tissue volumes up to one cubic millimeter with morphologically realistic cells reconstructed from electron microscopy [6]. The resulting models enabled the evaluation of the effects of microscopic E-field perturbations on neural activation thresholds in response to, for example, transcranial magnetic stimulation [6–9] and sparked constructive debates about the uses and limits of microscopic models [4, 8–10]. We summarize and extend these discussions and outline a path toward coherent multiscale modeling frameworks of E-fields and neural activation generated by brain stimulation that span the micro-, meso-, and macroscales [4].

We start by defining the range covered by the mesoscale in the context of brain stimulation and describe why conductivity variations on this scale influence stimulation thresholds. We then summarize the status and challenges of macro- and microscale approaches that have potential to inform mesoscopic conductivity estimates. In the main part of the paper, we tackle the current lack of suitable 3D microscopic datasets by introducing an approach to estimate layer-specific mesoscopic conductivities from simulations of 3D blocks of simplified microscopic cellular representations informed by cell volume fraction data. Finally, we conclude by briefly summarizing the key points of this study.

2. Theoretical framework and previous work

2.1. Mesoscale and its relevance for brain stimulation

Microscale corresponds to sizes of cellular and subcellular structures in the range of nanometers to tens of micrometers. Macroscale, in the broader sense, refers to any tissue volume larger than microscale for which the underlying cellular composition can be locally homogenized. Depending on the model size and stimulation modality, macroscale can be considered on the order of several millimeters in size or larger, e.g. full head model for transcranial electromagnetic stimulation based on millimeter-resolution imaging data. In this context, the two orders-of-magnitude between the microscale and macroscale are considered the mesoscale. In other cases, e.g. deep brain stimulation or vagus nerve stimulation with implanted electrodes, macroscale corresponds to sizes of the electrode and subcortical nuclei or fascicle, which is similar to mesoscale for a full head model, and there may be a less clear distinction between macro- and mesoscales.

Head models implemented with the finite- or boundary-element method typically assign constant conductivity to each tissue volume, constrained by computational cost and the lack of spatially distributed measurements. Macroscopic E-field models almost always use homogenous conductivities despite being capable of simulating inhomogeneity, and the term ‘macroscopic’ may be conflated with ‘homogenous’ in modeling work [9]. Mesoscale conductivity also represents averages of microscopic cellular composition, in contrast to microscopic models that explicitly represent underlying cellular structures. Measurements of mesoscopic inhomogeneities, such as layer- or depth-dependent conductivities (or, equivalently, resistivities) in the cerebral, cerebellar, and hippocampal cortices [11–15] and in the retina [16–18], are available but rarely modeled [19, 20]. An important exception is white matter anisotropy modeled from diffusion tensor imaging data: the conductivity tensor varies on the mesoscale, although its magnitude is usually derived from a fixed equivalent isotropic conductivity value [21]. Major challenges also remain regarding partial volume effects at tissue boundaries due to the limited spatial resolution and lack of consensus on diffusion-conductivity mappings [21, 22].

Mesoscopic conductivity variations in macroscopic models are expected to affect the E-field [23] and hence activation thresholds [20], as the E-field can vary over distances comparable or larger than neuronal length constants. The mesoscopic E-field variations led to changes in activation thresholds of up to 30% in specific neuron models [9]. In contrast, microscopic E-field variations are spatially filtered by the neural membranes and average out on the mesoscale to mean values [10] that depend on the underlying cellular density and extracellular volume fraction [9]. Accounting for the microscopic structure [4], a model captured variations in the gray matter effective conductivity not only across layers but potentially also over short distances along the cortex within the same layer [9]. However, the assumption of such strong within- and across-layer conductivity variations needs to be experimentally validated, due to the modeling method simplifying the extracellular space as discussed below. Given the importance of mesoscale conductivity variations for E-field and neural simulations, we

outline approaches bridging micro- and macroscale data to derive mesoscale conductivity distributions. Here we focus on low-frequency, quasistatic conductivities relevant for transcranial electrical and magnetic stimulation [24]; frequency-dependent and non-ohmic aspects of tissue impedance are important but largely separate from the mesoscale spatial questions highlighted here.

2.2. Macroscale approaches

Higher resolution imaging can inform tissue models that capture mesoscale features, including meninges, large blood vessels, cortical layers, nuclei, or other variations in tissue properties within brain regions, and even microscopic structures within a region of interest [25]. However, electrical properties are mostly measured on macroscales and distributions on the mesoscale are not available for most tissue types. Conventional metal microelectrodes and electrode arrays for impedance measurements average conductivity over relatively large volumes [17], whereas fine-tipped ($\sim$1 μm) glass micropipettes can resolve fine conductivity changes (figures 1(A) and (B)). Unlike the sharp tissue conductivity boundaries represented in models, actual transitions of tissue composition (e.g. from gray matter to white matter) are smoother [19, 26] (figure 2(A)). Therefore, measurements must distinguish true conductivity gradients from artifacts introduced by the electrodes and tissue preparation (figure 1(B)). Applying macroscale electric impedance tomography principles to multi-electrode arrays [27, 28] could measure mesoscale conductivity distributions within brain tissue samples *in vitro* (figure 1(C)). Such systems require dense electrode coverage and careful calibration. Alternatively, multi-contact electrodes [14, 23] can measure spatial E-field profiles during local microstimulation [29] or transcranial stimulation [23], informing conclusions about mesoscale conductivities and their spatial variations.

2.3. Microscale approaches

Microscale variations in tissue conductivity can be modeled using simplified geometries [34, 35] and extracellular volume fraction data [36] or realistic tissue structure from electron microscopy [4, 9, 20, 37]. However, most electron microscopy methods, including those used in recent large-scale connectomics projects [26, 32], rely on chemical fixation, which causes tissue shrinkage and distortions of cellular structure due to dehydration [31, 38, 39]. Chemical fixation results in an almost complete absence of the 40–80 nm wide extracellular gaps between cell membranes [40], leading to direct contact between neighboring membranes [31] and underestimation of the extracellular volume fraction (figure 2(B)). This issue is mitigated in tissues processed with cryofixation, but to what extent the reconstructed cells are free from distortion is unknown. In recent microscopic E-field models [6, 7, 37], the tissue had a volume fraction of 'extracellular space' of around 40%–70%, larger than the 15%–30% range obtained from *in vivo* diffusion studies [36]. This discrepancy appears to arise because the model's 'extracellular space' subsumed intracellular regions of omitted cell structures (e.g. neurites belonging to somata outside the sample, blood vessels, and neuroglia including myelin; figure 2(C)). Thus, although these microscopic models provide valuable insight into E-field distortions around complex cellular (or vascular) morphologies, the uncertainties of extracellular space limit the use of these models for conductivity estimation. Super-resolution optical microscopy enables nanoscale reconstruction of brain tissue in living samples while avoiding fixation- or freezing-induced artifacts [41], but these methods are limited to shallow depths due to light scattering and are still not viable *in vivo*. With enhancements of these techniques, structural imaging could be combined with physiological measurements in the same preparation to build microscale reconstructions that accurately capture the extracellular space and enable accurate determination of micro- and meso-scale tissue conductivities.

2.4. Modeling layer-specific cortical conductivity

Laminar probe measurements during transcranial electrical stimulation revealed marked variation in E-field amplitude across cortical layers [23]. Under the approximation that the macroscopic current density beneath the large surface electrodes is relatively uniform, this indicates conductivities vary substantially between cortical layers. Therefore, obtaining layer-specific conductivity measurements in the cortex would improve modeling accuracy, especially for invasive stimulation using electrodes for which the local field gradients are high. To obtain mesoscopic conductivity values from microscopic cellular structures, we examine how the conductivity of neural tissue varies as a function of cell density and thus volume fraction using computational models. As layer-specific cellular volume fractions are not directly available, complementary volume fractions of extracellular space from diffusion experiments were used. The goal of the present modeling analysis is not to produce definitive cortical conductivity values, but to quantify how strongly effective conductivity depends on extracellular volume fraction under controlled microscopic geometries, and to demonstrate how layer-specific volume-fraction data can be mapped to provisional layer-specific conductivities.

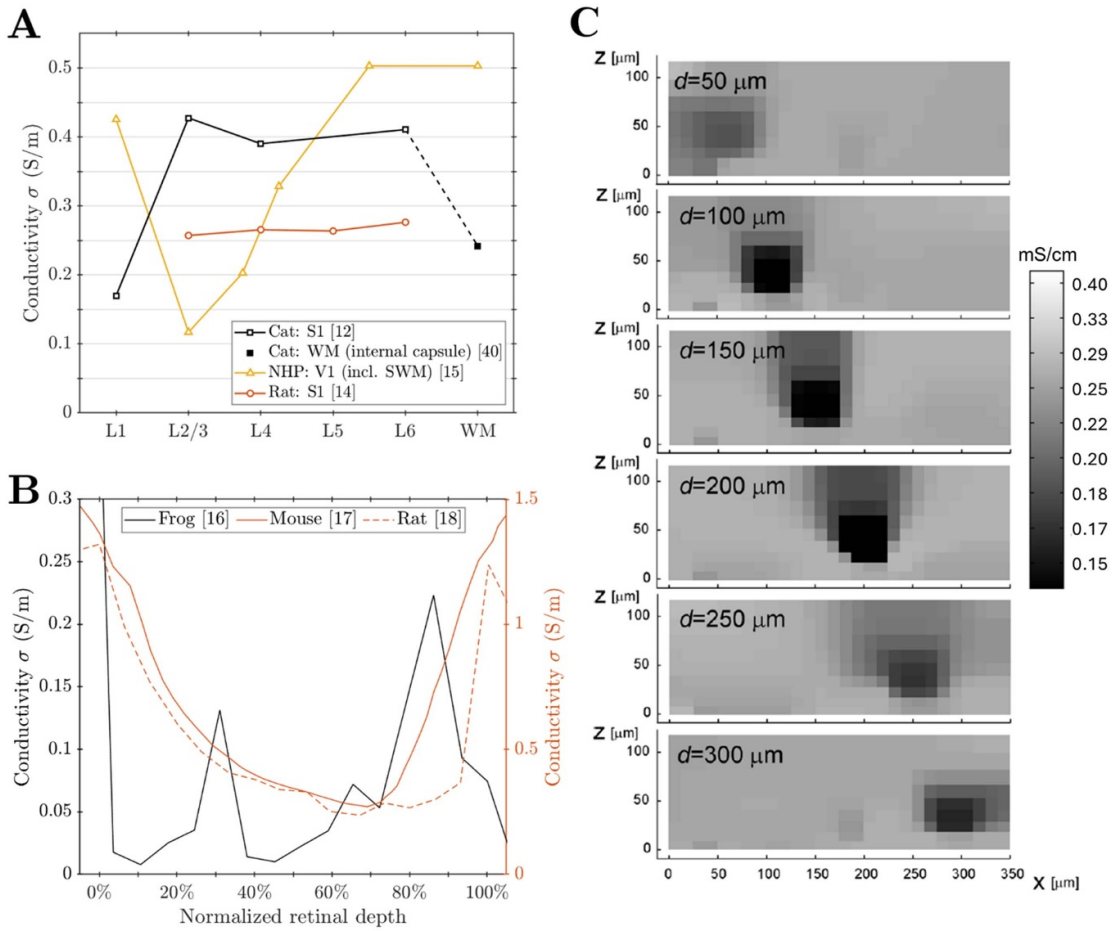

Figure 1. Approaches and results for measuring mesoscopic conductivity distribution. (A) Comparison of conductivity of cortical layers and white matter (WM) from different studies: (i) equivalent isotropic conductivity of gray matter measured in the cat somatosensory cortex (black squares) using glass micropipettes [12], with layer 5 data not collected, and equivalent isotropic conductivity of white matter measured in the cat internal capsule (black diamond) using a wire probe [30]. (ii) Equivalent isotropic conductivity of gray matter measured in the rat somatosensory cortex (orange circles) using electrode arrays [14]. (iii) Radial conductivity of gray matter and superficial white matter (SWM) estimated in the visual cortex of non-human primates (NHPs) (yellow triangles), from potentials generated by transcranial alternating current stimulation and measured with linear electrode arrays [15], with layers 5 and 6 considered as single layers and layer 4 subdivided into L4AB and L4C. (B) Depth-dependent resistivity of the retina, with normalized depth of 0% indicating the retinal ganglion cell side and 100% indicating the photoreceptor side. (i) Measurements using micropipettes with sub-micrometer diameter in a frog eyecup (left axis, black line) show distinct conductivity variation with depth and much lower values due to the intact retinal pigment epithelium [16]. (ii) Measurements using microelectrodes in isolated rodent retina without the highly-resistive retinal pigment epithelium show higher conductivity and smooth profiles that average the conductivity of distinct layers and surrounding saline due to spatial averaging of the electrodes and tissue distortion and disruption during electrode insertion [17] (right axis, orange lines [17, 18]). (C) Electric impedance tomography performed with an electrode array of 5 μm wide planar electrodes can resolve the position of a 45 μm diameter hair and obtain conductivity distribution maps with 10 μm resolution [28]. Panel (C) © (2008) IEEE. Reprinted, with permission, from [28].

3. Methods

3.1. Theoretical formulas for conductivity-cell volume fraction relationship

Previous studies [42–47] modeled the relationship between effective conductivity σ and volume fraction of cells f (table 1 and figure 3). Most methods assumed a low volume fraction for cell suspensions, with the conductivity of the extracellular fluid as σ_0 and homogenous cell conductivity, which for simplicity can be set to zero given the extremely low conductivity of cell membranes. Maxwell's formula [42] was derived by considering an infinite medium with uniform current flow, in which conducting spherical cells are suspended within a spherical volume. The boundaries of the cells each generate a secondary E-field, and their combined far-field potential can be given by linear summation, assuming the interactions between them are negligible and differences in their location are small relative to the far-field distance. Similarly, the far field potential can also be given for the spherical volume assuming a homogeneous conductivity different from the medium. By comparing these two potential expressions and making them equivalent, the effective conductivity of the cell suspension is derived. Due to the lack

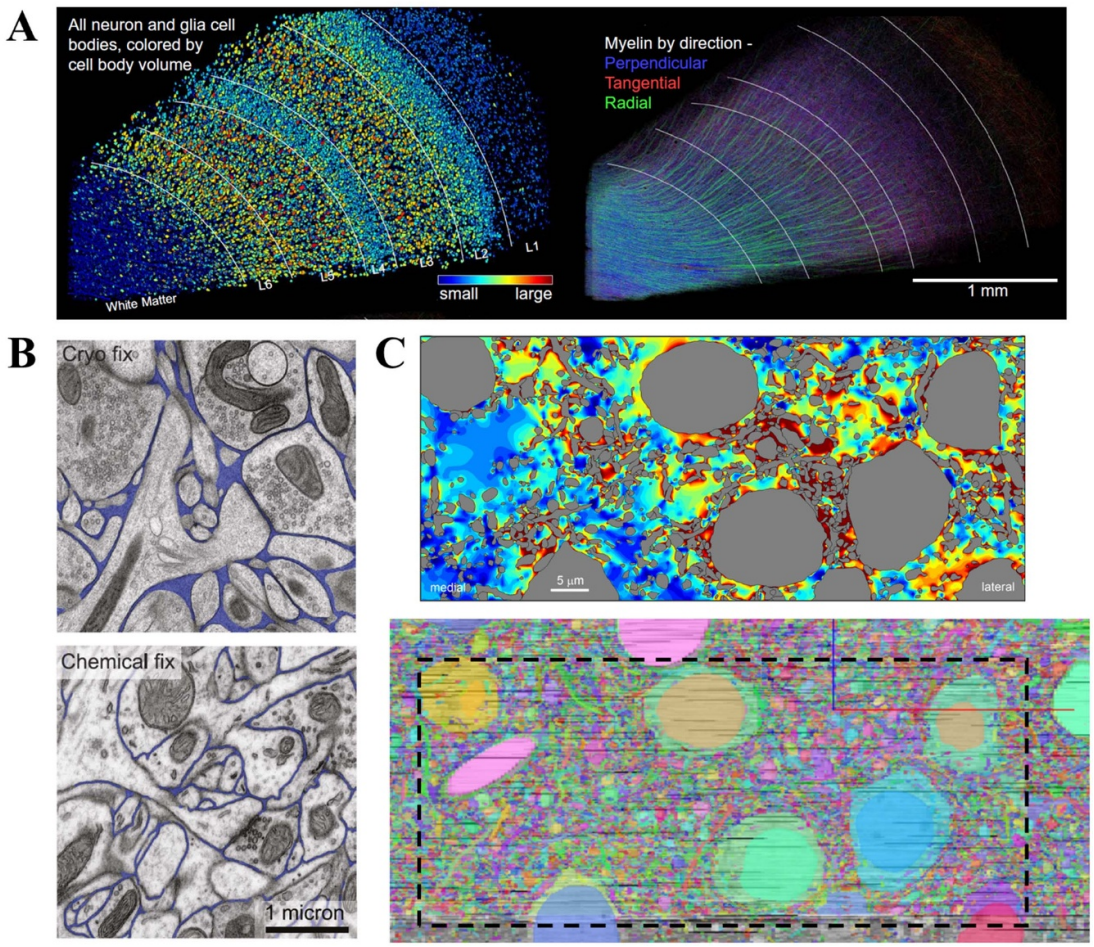

Figure 2. Microscopic tissue structures and challenges with accurate capturing of extracellular space. (A) Spatial extent of layers with different tissue structure in cortex. Distributions of neuron somas and glia cell bodies (left) and myelinated fibers (right) reconstructed from nanometer-resolution electron microscopy show transitions between cortical layers and gray and white matter regions over the mesoscale of tens to hundreds of micrometers [26]. (B) Electron microscopy images of tissue processed with cryofixation (top) and chemical fixation (bottom) show significant difference in extracellular space (pseudo-colored in blue) among other fixation-induced changes [31]. (C) Top: microscopic E-field simulation [6, 7] showing large extracellular space (color map showing E-field) with ∼70% volume fraction and small intracellular space (gray) of ∼30% volume fraction. Bottom: electron microscopy of the MICrONS dataset of mouse visual cortex [32] on which the microscopic E-field simulations were based showing the same frame (dashed outline). The micrograph reveals dense cellular and subcellular composition (filled with random colors) with almost no extracellular space due to chemical fixation. Panel (A) From [26]. Adapted with permission from AAAS. Panel (B) Adapted from [31]. CC BY 4.0. Panel (C) Top part adapted from [7], Copyright (2025), with permission from Elsevier. Bottom part from [33].

of shielding between cells, their secondary fields are much stronger than they would be with intercellular interaction and resulted in a much lower total field. Therefore, Maxwell's formula substantially underestimated the conductivity, having an initial slope twice as steep compared to later formulas for low volume fractions. The work by Lord Rayleigh [43] and later improvements by [44, 45] considered the spheres arranged in a simple cubic lattice and cylindrical cells in a square lattice and calculated the interactions of the E-fields from closest neighbors within a certain distance. This method provided better conductivity estimates; however, it has two limitations: (1) the maximum tissue volume fraction is limited to relatively low values (52.4% or 78.5% for simple cubic and square lattices, respectively) compared to those in the brain, especially for representation of cell bodies. (2) The current in square grids and cubic lattices mainly flows along uninterrupted straight lines and flat planar sheets respectively between the cells and therefore these geometries are poor representations of the tortuous paths in real tissue.

3.2. Layer-specific volume fraction of extracellular space and cells in brain

We used the volume fraction of extracellular space, α, obtained by Lehmenkühler *et al* with *in vivo* diffusion methods in somatosensory cortex and subcortical white matter of adult rats (table 2) ([36, table 1]). In

Table 1. Theoretical formulas describing the relationship between tissue conductivity (σ) relative to extracellular fluid conductivity (σ_0) as a function of cell volume fraction (f) for various tissue structure scenarios assuming non-conducting cells.

Formula	Notes	Sources
$\frac{\sigma}{\sigma_0} = \frac{1-f}{1+2f} = 1 - \frac{3f}{1+2f}$	Dilute cell suspension	[42] (Part II, Ch. IX, Section 314, equation 17)
$\frac{\sigma}{\sigma_0} = \frac{1-f}{1+f/2} = 1 - \frac{3f}{2+f}$	Spherical particles arranged in a simple cubic lattice, $f < 0.524$	[43] (equation 68)
$\frac{\sigma}{\sigma_0} = 1 - \frac{3f}{2+f-0.394 \cdot f^{\frac{10}{3}}}$	Spherical particles arranged in a simple cubic lattice, higher order approximation, $f < 0.524$	[43] (equation 80, corrected by [44])
$\frac{\sigma}{\sigma_0} = 1 - \frac{3f}{2+f-\frac{0.986 \cdot f^{\frac{10}{3}}}{1-0.307 \cdot f^{\frac{7}{3}}}}$	Spherical particles arranged in a simple cubic lattice, next higher order approximation, $f < 0.524$	[45] (equation 16)
$(1-f)^{\frac{5}{3}} \leq \frac{\sigma}{\sigma_0} \leq (1-f)^{\frac{3}{2}}$	Elongated homogeneously distributed randomly orientated spheroids	[46] (equation 14)
$\frac{\sigma}{\sigma_0} = \frac{1-f}{1+f} = 1 - \frac{2f}{1+f}$	Parallel cylindrical cells in square grid, $f < 0.785$	[43] (equation 35, simplified)
$\frac{\sigma}{\sigma_0} = 1 - \frac{2f}{1+f-0.306 \cdot f^4}$	Parallel cylindrical cells in square grid, $f < 0.785$	[43] (equation 35, higher order approximation)
$\frac{\sigma}{\sigma_0} = \begin{cases} (1-f)^1 \\ (1-f)^2 \end{cases}$	Parallel fibers, longitudinal parallel fibers, transverse	[46] (equation 3)

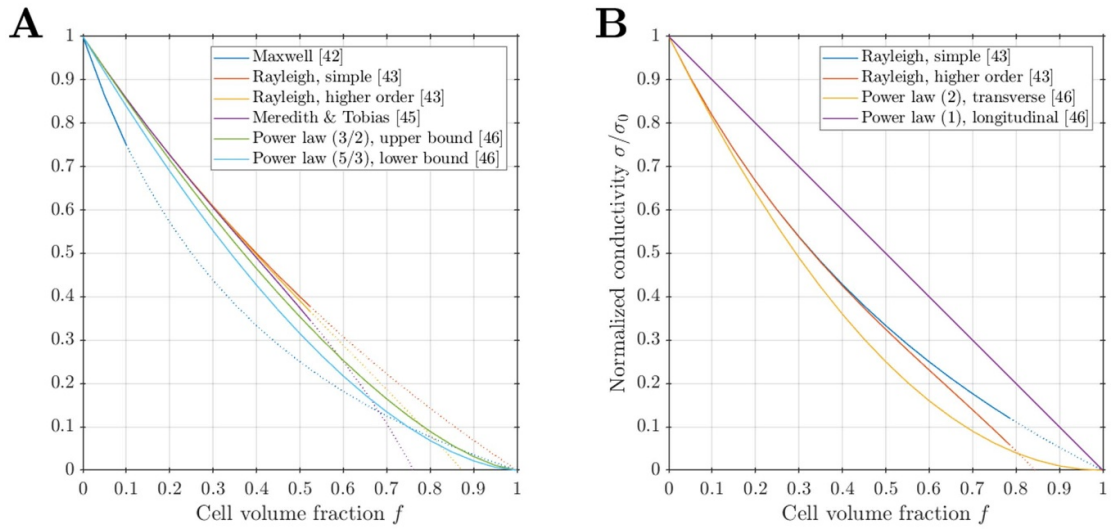

Figure 3. Theoretical formulas for effective conductivity of spherical or spheroidal cells (A) and parallel axons (B) normalized to extracellular conductivity. Relationships derived for lattice formation are shown with a solid line to the upper limit of the volume fraction, with extrapolation given in dotted lines. Maxwell's formula was similarly given with an upper limit of 10% for consideration of dilute cell suspension.

summary, tetramethylammonium concentration was measured with ion-selective microelectrodes positioned 130−200 μm from an iontophoretic source and diffusion equations were fit to the concentration versus time assuming spherical symmetry to extract parameters including α, tortuosity, and cellular uptake. The volume fractions of cells were given as $f = 1 - \alpha$.

3.3. Tissue models and simulation setup

3.3.1. Common model setup

We built cubic blocks of simplified microscopic cellular representations of several tissue types (figure 4) using finite element models in COMSOL Multiphysics (version 6.3, COMSOL, Inc.) on a desktop workstation (Intel Core i7-7800X, 128 GB RAM). Three tissue types were modeled, parallel axons (2D), cell bodies (3D), and interleaved neurites (3D), with specific details for each type described below. The unit cell for the 2D grid or 3D lattice of all tissue types had a side length d of 10 μm, and the 2D and 3D tissue blocks were cubes with side length of 18 and 6 times d, i.e. 180 μm and 60 μm, respectively. Conductivities of cell membranes and the intra- and extra-cellular spaces were assigned with typical values according to literature (table 3). The cell volume fraction was swept in steps of 5% from 5% up to 95% or the maximum allowed by the specific tissue model (see appendix table A1), and the cell sizes were varied accordingly. Different cell shapes and orientations of the tissue structure were modeled to quantify their influence on the conductivity. In addition

Table 2. Measured volume fraction of extracellular space [36, table 1] and cells (mean and standard deviation).

Layer	Volume fraction of extracellular space, α	Volume fraction of cells, f
L1	Not available	Not available
L2	19% ± 0.2%	81% ± 0.2%
L3	20% ± 0.4%	80% ± 0.4%
L4	21% ± 0.3%	79% ± 0.3%
L5	22% ± 0.3%	78% ± 0.3%
L6	23% ± 0.7%	77% ± 0.7%
White matter	20% ± 0.8%	80% ± 0.8%

to cylindrical or spherical shapes, we also explored polyhedral geometries which did not have limits on volume fraction.

The models used triangular and tetrahedral elements for 2D and 3D models, respectively, with COMSOL's physics-controlled setting of 'finer' for meshing. Mesh convergence was tested with increased or decreased mesh resolution ('extra fine' or 'fine' settings) confirming sufficient accuracy with negligible (<1%) changes of the results (see appendix table A2 for details of mesh settings). Simulation time varied between 10 s and 3 min for different combinations of volume fraction and orientation of 2D tissue models, and from 30 min to over 5 h for each combination of volume fraction and rotation of 3D models. The model tissue block sizes were chosen to be large enough that the underlying cellular structures could be homogenized on the scale of the block, while at the same time not being too large to become computationally prohibitive (memory limited). In a test with a slightly larger block size (70 μm side length) and a few sampled volume fractions for 3D models, the effective conductivity had minimal changes (<1%). We did not explore the minimum block size that would allow accurate estimation.

The potential and E-field distributions were simulated for 1 μA current applied on one side of the sample with a floating potential boundary condition [48], with the opposite side grounded. To avoid direct contact between the electrodes and cells, small gaps (each with width 0.5% of the tissue block size, i.e. 0.9 μm and 0.3 μm for 2D and 3D models, respectively) were added. The floating potential enforced the equipotential boundary condition on the electrode surface and allowed the given total current to distribute nonuniformly across the boundary. The resistance was calculated by dividing the floating potential sampled from an arbitrary point on the electrode surface by the total current; this approach was easier compared to performing surface integration of the current for a fixed voltage boundary. The remaining four sides of the tissue block were insulated, including the boundaries of the extracellular space and the intersections of the block with cells[10]. Although the cells near the boundaries of the tissue block were artificially cut and incomplete, they did not affect simulation accuracy given their negligible proportion compared to the interior and the symmetry of the system in the direction transverse to the current flow. The resistances of the two extracellular gaps were subtracted from the total resistance to obtain the resistance of the tissue block. The effective tissue conductivity was then calculated for a given tissue type and averaged for various cell shapes and rotational orientations of the tissue structure. The conductivities of different cortical layers (layers 2–6) were interpolated based on experimental volume fraction in the range of 70%–90%. Data analysis and additional visualization were conducted in MATLAB (version 2024b, The MathWorks, Inc).

3.3.2. Parallel axons

Cylinders and hexagonal prisms [49, 50] placed in hexagonal grids were used to represent parallel axons (figure 4(A) and appendix figure A1 and table A1). Compared to square grids [43], hexagonal grids eliminated any straight current paths through the tissue block. Circular cross-section allowed cell volume fractions up to 90.7%, whereas hexagonal prisms allowed denser packing theoretically achieving 100% volume fraction. The maximum volume fraction that was modeled for the former was 90% to avoid direct contact between cells that would completely pinch off the extracellular space and therefore result in zero conductivity due to negligible transmembrane and intracellular currents. Given the longitudinal symmetry along the axons' axes, a 2D model was built with the axial direction not explicitly represented. The orientation of the grid pattern was rotated up to 30° in steps of 5° as a second parameter sweep.

3.3.3. Cell bodies

Spheres [47] and truncated octahedrons [51] placed in body-centered cubic lattice were used to represent tight packing of cells (figure 4(B) and appendix figure A2 and table A1), with the former being limited to a volume fraction of 68.0%. Unlike the 2D case, spheres on a 3D body-centered cubic lattice retained a connected extracellular space at contact, so current pathways remained available at the contact volume fraction. Three tissue orientations were used, corresponding to lattice Miller indices of [100], [110], and

[10] A periodic boundary condition could also be used on these four sides, i.e. so that the solver matched the potential and current on corresponding locations of opposite sides. This setup would implicitly represent the same block being repeated in space and therefore require a much smaller block size in the transverse direction to only include one unit cell. However, this would require adjusting the block size for different rotations of the tissue so that the boundary meshes on opposite sides could be matched for all parameter settings.

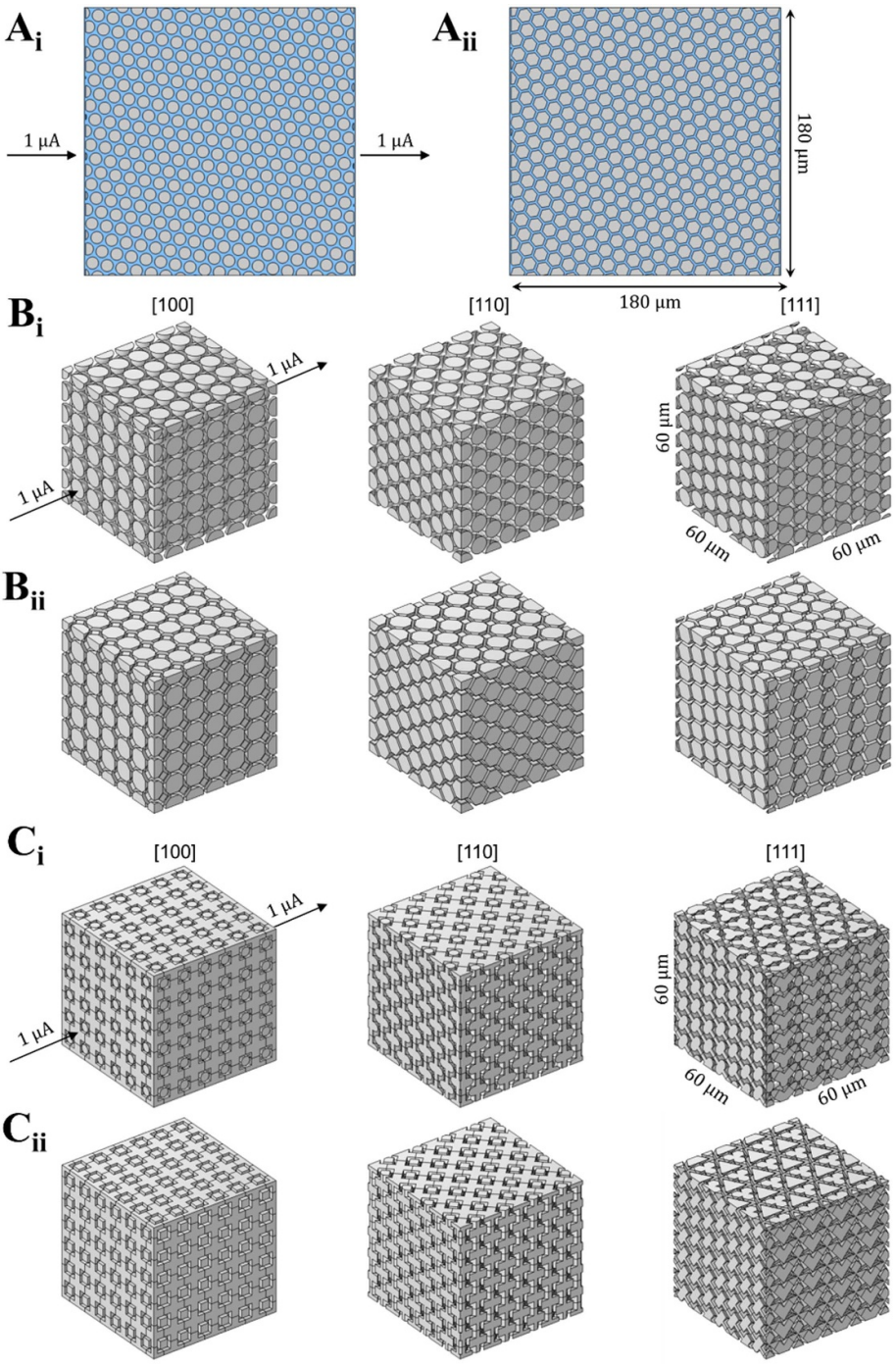

Figure 4. (A) Axons transverse to the current direction modeled as hexagonal grids of cylinders (A_i) and hexagon prisms (A_{ii}). The 2D model had an implicit depth of 180 μm. The axon grids had a cell volume fraction of 60% (4.1 μm radius) and 70% (4.8 μm side length) and rotation of 10° and 20°, respectively. The extracellular space is shown in blue. (B) Cells modeled as body-centered cubic lattices of spheres (B_i) and truncated octahedrons (B_{ii}). The current was aligned with the [100] (left), [110] (middle), and [111] (right) orientations of lattices, all with a cell volume fraction of 60% (4.2 μm radius and 3.0 μm side length, respectively). The extracellular space is not shown. (C) Interleaved neurites modeled as body-centered cubic lattices of 3D-crosses of circular (C_i) and square (C_{ii}) cross-section, with cell volume fraction of 60% (2.1 μm radius of circular cross section and 3.6 μm side length of square cross section, respectively).

Table 3. Model parameters.

Parameter	Symbol	Value	Unit
Extra- and intracellular conductivity	σ_0	1	$S{\cdot}m^{-1}$
Membrane conductivity	σ_m	10^{-8}	$S{\cdot}m^{-1}$
Membrane thickness	t_m	10	nm
Specific membrane resistance	R_m	1	$\Omega{\cdot}m^2$
Unit cell side length	d	10	μm

[111], i.e. planes normal to the cubic axis, face diagonal, and body diagonal directions. Unlike the simple cubic lattice used in previous studies [43], the body-centered cubic lattice did not have continuous planar corridors for current flow across the entire tissue block. Although isolated straight axial paths were still present, they occupied a small fraction of the cross-sectional area and current would be instead carried predominantly through the interconnected oblique gaps between neighboring cells.

3.3.4. Interleaved neurites (neuropil)

3D-crosses with circular and square cross-sections placed in body-centered cubic lattice were used to represent densely interleaved neural branches in the neuropil (figure 4(C) and appendix figure A3 and table A1), with the 3D model setup similar to that of the cell bodies. The volume fraction for circular cross-sections had an upper bound of 82.5%. Unlike the previous convex morphologies, the 3D-crosses were concave like real cells. The interconnection and interleaving were a simplified representation of the interactions between dense branches of cortical neurons. Although individual neurons have tree-like (acyclic) morphologies, networks of synaptically connected neurons form complex connectivity patterns. The interlinked 3D-cross structures provided a topological and electrical abstraction of such dense interdigitation. As explicitly resolving nanometer-scale gaps representing synaptic clefts would require prohibitively fine mesh elements, the opposing membranes of adjacent crosses were fused together where they would otherwise come close together. For the present objective of estimating bulk tissue conductivity, the fused-membrane approximation therefore neglected narrow local conductive pathways while preserving the dominant pathways through the larger extracellular spaces between neighboring structures that governed the homogenized tissue conductivity.

4. Results

4.1. Field distributions

The potential distribution varied linearly and continuously from one electrode to the other in the extracellular space given the translational symmetry of the system in the direction of the current flow[11] (figure 5, first row); in contrast, the E-field was approximately zero (<1 mV m^{-1}, figure 5, third row) inside the cells due to the highly resistive membrane and due to the membrane charges resulting in transverse/initial polarization [52, 53] almost completely cancelling out the imposed primary E-field on sub-microsecond time scales. Therefore, the intracellular potential at 'steady state' was constant and equal to the extracellular potential averaged across the membrane[12] [53]. This is best illustrated by subtracting a linear potential distribution for homogenous space, revealing that residuals in the extracellular space were zero but varied linearly in the intracellular space (figure 5, second row), with minor perturbation from zero at the insulating boundaries where cells were artificially cut and the symmetry was broken.

4.2. Effective conductivity

The effective conductivities calculated from the total resistance of the tissue blocks for a given cell volume fraction were averaged across different orientations of the tissue structure relative to the main direction of the E-field (figure 6). The coefficient of variation for each combination of tissue type and cell volume fraction was less than 0.03, showing that the orientation of the tissue structure had no impact on the effective conductivity. Further, the conductivity of different cell shapes for the same tissue type agreed with each other, indicating that the effective-conductivity-volume-fraction relationships were mostly not affected substantially by cell shape either. Compared to the effective conductivity of polyhedral cell shapes, those of cylindrical axons and spherical cells deviated downward near the limits of their volume fractions. These deviations were due to the curved membranes having extracellular space with irregular shape and smaller gaps with non-uniform width. Especially, the conductivity of cylindrical axons dropped to zero approaching their volume fraction limit, whereas those of 3D structures had a non-zero value.

[11] The anodal half of the space should have half the potential drop between the electrodes. Otherwise, if the potential drop were different, say larger, than half the total, 'copying' and translating this half of space to the cathodal side would result in a potential drop larger than the total. Applying this argument, the potential at any location along the current flow should be linear with the distance from the floating potential to the ground.

[12] For complex neural morphology, transverse/initial polarization occurs across each cross section of the neural cable, resulting in an intracellular potential that is uniform within the cross section but varies longitudinally along the cable. This axial potential distribution drives neural activity in response to extracellular stimulation. See sections 2.1 and 2.2 of [53] for a full discussion. On time scales larger than the cell's time constant, e.g. transcranial direct current stimulation, equilibrium is also reached for the intracellular potential axially across the entire cell, and the transmembrane potential for subthreshold polarization can be obtained with the mirror estimate [61].

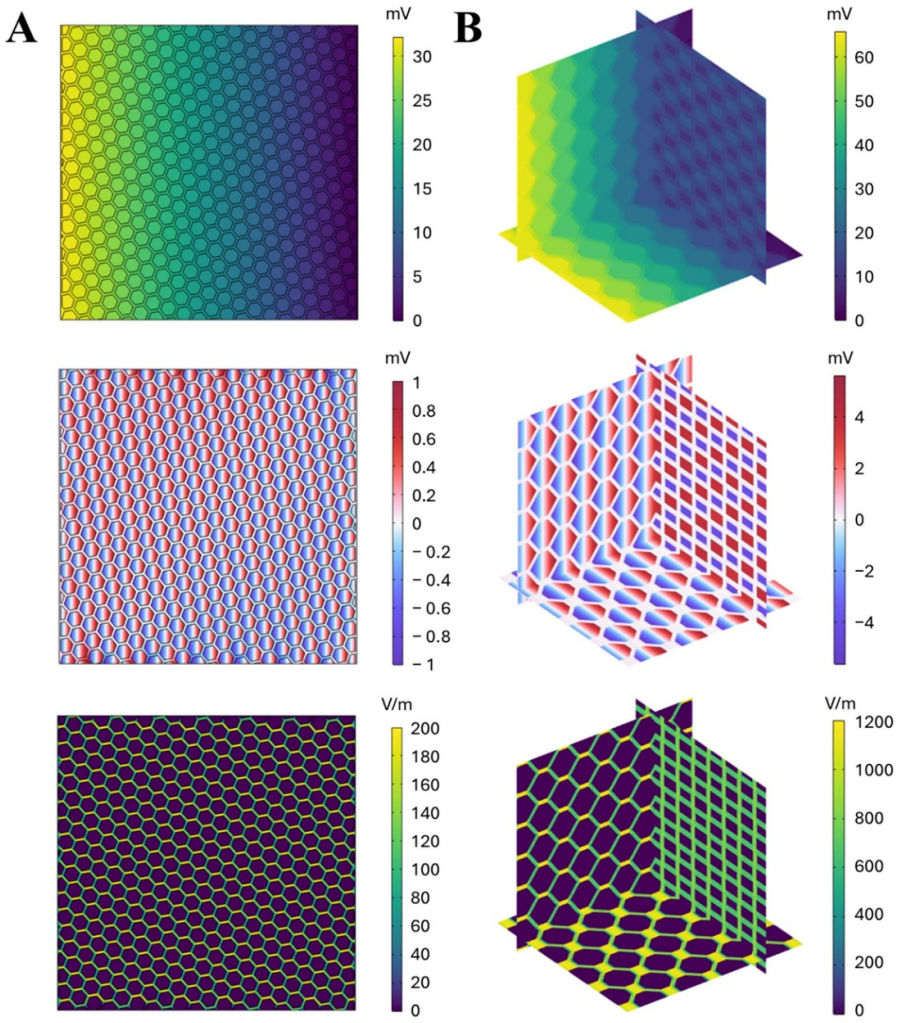

Figure 5. Example distributions of potential (first row), residual potential from secondary field of bound membrane charges after subtracting a linear potential (second row), and E-field amplitude (third row). The extracellular potential changes linearly between the two electrodes, whereas the intracellular potentials are constant and equal the extracellular potential averaged across the cell membrane. (A) 2D model of hexagonal axon grid with 70% cell volume fraction and 20° rotation. (B) 3D model of truncated octahedron cells with 65% cell volume fraction and [110] Miller index orientation, with three orthogonal slices shown.

The effective tissue conductivities for the three modeled tissue structures were monotonically decreasing convex functions of the cell volume fraction. They followed the theoretical power formulas [46] only for small volume fractions (<20%) and deviated to higher values for larger volume fractions. Surprisingly, Rayleigh's simple approximation formulas without the higher order correction terms matched the relationship for cell bodies and axonal transverse conductivity in the entire range of volume fractions, and their mean followed interleaved neurites closely (figure 6). This was potentially due to the hexagonal grid and body-centered cubic lattice mostly eliminating uninterrupted straight current paths through the tissue block present in the square grid and simple cubic lattice used by Rayleigh, therefore better homogenizing the current flow and not needing the higher order correction terms.

We analyzed the sensitivity of the effective conductivity to the volume fraction using the theoretical formulas by Rayleigh, given their strong match with the simulation results. The relative sensitivity $\kappa(f) = \frac{f}{\sigma}\frac{\mathrm{d}\sigma}{\mathrm{d}f}$ was evaluated for f between 0.75 and 0.85, the volume fraction relevant to brain tissue (table 2) [36]. For parallel axons, the conductivity was described by $\sigma_{\mathrm{axon}}(f) = \sigma_0(1-f)(1+f)^{-1}$ and therefore $\kappa_{\mathrm{axon}} = -\frac{2f}{1-f^2}$. For a 1% change in volume fraction at $f = 0.8$, the effective conductivity would change by −4.4%. This agreed with the simulation results, e.g. a ± 0.05 or ± 6.25% change in volume fraction for $f = 0.75$ and 0.85 resulted in conductivity changes of ∓ 27.8%. Similarly, the sensitivity for cell bodies with $\sigma_{\mathrm{soma}}(f) = \sigma_0(1-f)(1+f/2)^{-1}$ was $\kappa_{\mathrm{soma}} = -\frac{3f}{(1-f)(2+f)}$ and slightly lower (e.g. −4.3 at $f = 0.8$). The high sensitivity (−3.3 to −6 for volume fractions between 0.75 and 0.85) indicated

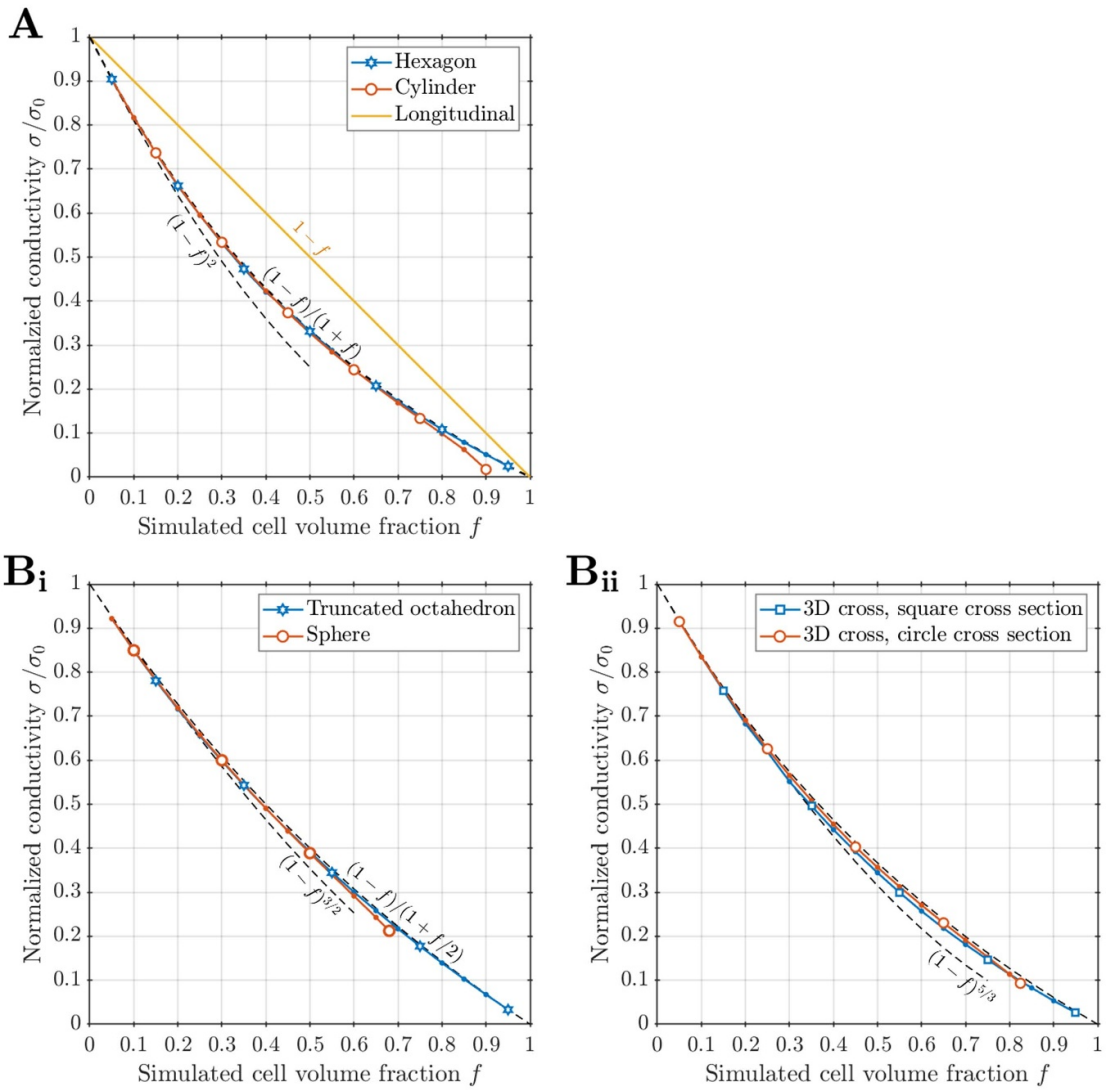

Figure 6. Effective tissue conductivity normalized to extracellular fluid as function of volume fraction and averaged across orientations. (A) 2D models (average of 7 orientations). (B) 3D models (average of 3 orientations) representing cell bodies (B_i) and interleaved neurites (B_{ii}). Except near packing limits, the conductivity–volume-fraction relationships were similar for the tested cell shapes, as demonstrated by the overlapping lines for the same tissue type. Some theoretical formulas are also plotted as dashed lines, with the unmarked line in panel B_{ii} representing the average of the two corresponding formulas in panels (A) and B_i. Markers are not shown at all data points to avoid overlap, with the maximum volume fractions modeled all marked.

that conductivity contrasts were larger than assumed from a linear relationship [9], especially for higher volume fraction. The effective conductivity was proportional to the extracellular conductivity, and therefore the relative sensitivity was 1, i.e. a 1% change or uncertainty in extracellular conductivity results in a 1% change in the effective conductivity.

4.3. Layer-specific conductivity

In the cortex and subcortical white matter, approximately 75% of the cellular volume consists of entangled elongated structures such as axons, dendrites, cilia, and blood vessels (see table S4 of [26]). Therefore, we interpolated the conductivity of each cortical layer from the simulated results for interleaved neurites (figure 6(B)) using the layer-specific cell volume fractions (table 2), with the results shown in figure 7(A). Here, the conductivity of the extracellular space was assumed to be cerebrospinal fluid, 1.8 S m^{-1} [54]. The conductivity of subcortical white matter was also estimated for isotropic and anisotropic cases, with the latter using the simulated results for transverse conductivity of parallel axons (figure 7(A)) and empirical formula for longitudinal conductivity (table 1).

With decreasing cell volume fraction, the conductivity of cortical layers increased with depth from layer 2 to layer 6 (figure 7(A)). Conductivity of layer 1 was estimated to be the lowest (0.14 S m^{-1} [19]), in agreement with this trend. Due to the high relative sensitivity, the conductivity difference between layers was considerably larger than their variation in volume

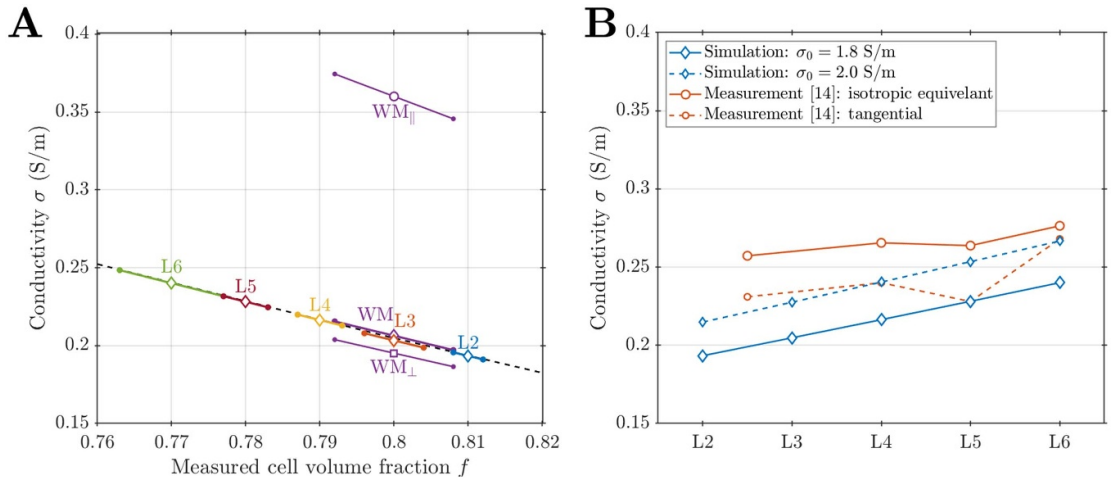

Figure 7. (A) Effective tissue conductivity of cortical layers shown according to their cell volume fraction, assuming σ_0 as 1.8 S m^{-1}. Markers are interpolated according to experimental data from [36], with line extensions indicating the variation corresponding to one standard deviation of the volume fraction, and results of L3 and white matter (WM) slight offset for clarity. The dashed line corresponds to simulated results for interleaved neurites (figure 6). White matter conductivity was also calculated for anisotropic and isotropic cases based on its volume fraction. (B) The layer-specific conductivity (blue diamonds, with the solid line corresponding to interpolated data in panel A and dashed line corresponding to estimates using slightly higher extracellular conductivity of 2 S m^{-1}) are compared to measurement in the rat somatosensory cortex ([14], orange circles, with solid line corresponding to equivalent isotropic conductivity as shown in figure 1(A) and the dashed line corresponding to conductivity measured in the tangential direction, i.e. parallel to the cortical surface).

fraction. For example, layers 3 and 6 were respectively around 5% and 24% more conductive than layer 2, despite their volume fraction being only 1.3% and 5% lower than that of the latter.

With high cell volume fractions, the simulated isotropic conductivity of subcortical white matter was lower than all layers except layer 2, although it should be noted there were substantial differences in the longitudinal and transverse conductivities as expected with anisotropy, with longitudinal conductivity of white matter measured as high as 1.1 S m^{-1} in some studies [30].

5. Discussion

In this work we first conducted theoretical analyzes of the spatial scales of tissue properties and E-field in brain stimulation, highlighting the importance of the mesoscale in accurate modeling. Approaches that estimate effective mesoscopic tissue conductivities from micro- and macroscales complement and validate each other and should converge on consistent mesoscale distributions. The technical challenges of these approaches include limited spatial resolution of the conductivity due to the size and number of the measurement electrodes and tissue deformation and shrinkage during chemical fixation for electron microscopy. These challenges need to be addressed via collaboration across different fields, including biophysics and physiology, electrode microfabrication, high resolution imaging, histology, and computational modeling. Further combining mesoscale models with physiological experiments could identify sufficient levels of biophysical detail for predictive models and validate statistical averaging across neurons within a tissue volume and across subjects.

Demonstrating the microscale approach, we built microscopic tissue models with simplified cell geometry to evaluate effective tissue conductivity using cell volume fraction data obtained from diffusion measurements. Compared to realistic cellular models obtained with electron microscopy, the simple models allowed precise control of the volume fraction of the cells and extracellular volume homogenized on the mesoscale, and circumvented issues of histology-derived models that include chemical-fixation-induced tissue shrinkage and have high computational costs. The translational symmetry of the simple cell shape and regular lattices also avoided issues of division of realistic tissue structure into non-overlapping blocks [9, 37], which could generate spurious strong conductivity contrast between neighboring blocks due to arbitrary block placement and would be smoothed out by having some overlap. For a given tissue type, the effective conductivity-volume-fraction relationships of the spatially symmetric models were not affected by orientation of the E-field relative to the tissue structure or the cell shapes we tested. Whether such cell shape independence holds for realistic cell morphologies should be further examined

with more complex models [26, 32]. Except for formulas by Rayleigh, prior theoretical results did not agree with the relationship at high volume fractions relevant for brain tissue.

We estimated layer-specific cortical and subcortical conductivity using an interpolation of the simulated effective conductivity for interleaved neurites and assuming the extracellular conductivity to equal that of the cerebrospinal fluid (figure 7). The relative difference in conductivity between the layers was substantial. The results qualitatively agreed with the higher E-field measured in layer 2/3 compared to those in layers 4 and 5/6 during transcranial alternating current stimulation in non-human primates [23], in which the large surface electrode resulted in relatively uniform current density in the cortex, and thus the E-field was inversely proportional to conductivity. The modeled conductivity also exhibited a similar trend across layers compared to the equivalent isotropic conductivity of gray matter measured in the rat somatosensory cortex (figure 7(B), orange circles [14], calculated from radial and tangential conductivities), albeit with slightly smaller absolute values. Such differences may be attributed to an underestimation of the extracellular/interstitial fluid conductivity by using that of cerebrospinal fluid for the effective extracellular conductive space. For example, if a higher conductivity of 2 S m^{-1} was used, the effective tissue conductivity across all layers would be linearly increased by 11% (figure 7(B), dashed blue line). Further variation in the conductivity profile could be due to layer-dependent differences in the conductivity of extracellular fluids. However, such mesoscopic variation of fluid conductivity, if present, could be even more difficult to measure experimentally compared to the effective tissue conductivity itself, and the uncertainty of extracellular conductivity would have lower impact on the effective tissue conductivity compared to that of the volume fraction. Another potential factor for the discrepancy between our simulation and measurement was misestimation of the volume fractions, which were fitted assuming isotropic diffusion although the iontophoresis pipette and ion-sensitive microelectrode were lowered in depth together and therefore predominantly captured the diffusion parameters in the tangential direction [36]. The experimentally measured tangential conductivities were lower than the radial ones [14] (figure 8(B), dashed orange line) and agreed better with the model results.

Most computational modeling frameworks are quasi-static with time-invariant tissue properties [24]. In our effective conductivity estimation, dynamic changes in the membrane conductance due to neural activity can be safely neglected, given that peak membrane conductivity during action potentials is at most 4 orders of magnitude higher than rest (e.g. $\sim$1 S·cm^{-2} versus $\sim$0.1 mS·cm^{-2} at rest, or $\sim10^{-4}$ S m^{-1} versus $\sim10^{-8}$ S m^{-1} for 10 nm thick membrane) and thus still 4 orders of magnitude smaller than that of physiological fluids ($\sim$1 S m^{-1}). Moreover, such high conductivity occurs only on a small fraction of the cell membrane (<1%) for a small fraction of time (mostly <1%, but up to 10% for high frequency bursting, e.g. $\sim$100 Hz). Dynamic changes in extracellular space volume fraction can occur on the time scale of milliseconds to seconds during neural activity. Shrinkage of extracellular space, up to −30% relative volume decrease corresponding to 7.5% increase in total cell volume fraction for $f = 0.8$, are driven by activity-dependent influx and efflux of ions (especially K^+) and subsequent uptake by glia cells (primarily astrocytes), which induce osmotic water influx and cell swelling [55–57]. Therefore, stimulation induced neural activity could alter the local tissue conductivity which potentially affects the stimulation E-field, thereby creating dynamic feedback. During natural sleep or under anesthesia, the interstitial space increases from $\sim$14% to $\sim$23% (about 60% relative change) to enhance exchange between cerebrospinal fluid and interstitial fluid and increase clearance of metabolic waste [58]. Although it is unclear which cell types contribute to this change, the −10% relative decrease in the total cell volume fraction corresponds to substantial increase in conductivity around 50%. Therefore, variations in experimentally measured conductivity could be affected by whether the animal was under anesthesia. This could also have implications for the choice of conductivity for modeling electroconvulsive therapy, which is administered under anesthesia. Further, cell membrane capacitance can be included in the model to arrive at frequency-dependent conductivity and capacitance, which can be then compared to measurements from literature [59]. This could be relevant for stimulation modalities using high frequency waveforms (e.g. >10 kHz), for which the reduced membrane impedance allows more current flow via the intracellular space and therefore decreases the effective tissue conductivity. Overall, how layer-specific conductivity affects the modeled E-field is specific to the stimulation modality and could have substantial variation depending on the source and invasiveness (e.g. intracortical microstimulation versus transcranial electromagnetic stimulation), which should be explored in future studies.

The tissue models had several limitations besides simplified cell geometry. Realistic tissue consists of a mixture of cell sizes and types, with irregular shapes and higher tortuosity[13] and require more complex cell morphology to represent the current flow. Importantly, the cell membrane is not convex and can have local concave indentation and even 'dead ends' for ion diffusion and current flow [60]. Realistic brain

[13] Defined as ratio of actual path length versus distance for a straight line.

tissue has high tortuosity (1.6–1.7 [36]) and therefore long and narrow current paths for a given volume fraction. Simple geometries cannot capture these features, e.g. truncated tetrahedrons, cubes, and mixture of convex shapes all have tortuosity between 1.1 and 1.2 [51], and they might overestimate the conductivity for a given volume fraction. Because cortical gray matter is dominated volumetrically by neurites/neuropil, we used the interleaved-neurite model as the primary scalar approximation. However, this ignores layer-dependent somatic density, vascular volume, myelination, and glial morphology. A more complete model would combine multiple morphological classes or derive the membrane geometry directly from artifact-minimized microscopy. The accuracy of the modeled cortical conductivity also depended on that of the volume fraction of the extracellular space, especially given the high sensitivity of effective conductivity with regard to the volume fraction. The experimental volume fractions used in this study were obtained from rat somatosensory cortex [36], and variation between individuals, species (e.g. rat, cat, and non-human primate), and cortical areas (e.g. somatosensory, motor, and visual cortices) should be considered when comparing results across different studies ([12, 14, 15], figure 1(A)). The volume fractions were calculated by fitting the measured ion concentration to isotropic diffusion equations, which did not account for anisotropy [36]. Therefore, anisotropic conductivity values could be obtained with improved experimental estimation of volume fractions and further modification of the models to use geometries with reduced or no symmetry (e.g. spheroids [46] instead of spheres) and mixture of different morphologies. Ultimately, realistic cell structure from electron microscopy without tissue deformation should be utilized to arrive at mesoscale conductivity distribution of different cortical layers and brain regions [26]. Ideally, models should be built using reconstruction of the tissue where extracellular space is preserved and on which the conductivity is measured to allow direct validation between models and experiments.

6. Conclusions

Despite the numerous challenges of both microscale and macroscale approaches, they should converge on consistent mesoscale distributions of tissue conductivity. We demonstrated a simple mathematical method to evaluate tissue conductivity using cell volume fraction data, which can be obtained from microscopic tissue samples. Overcoming technical and methodological challenges, the quality of E-field models and simulations of brain stimulation can be improved by accurate representation of tissue conductivity on the mesoscale, including within the gray matter and at the transition from gray matter to white matter. Tissue conductivities vary substantially between cortical layers, and using layer-specific values within the cortex could improve the accuracy of E-field models for brain stimulation.

Acknowledgment

This work was supported by the National Institute of Mental Health and the National Institute of Neurological Disorders and Stroke of the US National Institutes of Health under Grant Nos. R01MH128422 and U01NS126052. A. Thielscher was supported by the Lundbeck Foundation grant R313-2019-622. The content is solely the responsibility of the authors and does not necessarily represent the official views of the funding agency. Preliminary results were presented at the Neural Interfaces 2025 conference, Arlington, VA, USA, 12–14 June 2025 [62].

Data availability statement

All data that support the findings of this study are included within the article (and any supplementary files).

Conflict of interest

B Wang, T H Worbs, M A Hussain, A S Aberra, A Thielscher, and W M Grill declare no relevant conflict of interest. A V Peterchev has received patent royalties and consulting fees from Rogue Research; equity options, scientific advisory board membership, and consulting fees from Ampa Health; equity options, consulting fees, and travel support from Magnetic Tides; consulting fees from Soterix Medical; equipment loans from MagVenture; hardware donations from Magstim; and research funding from Motif.

Author contributions

Boshuo Wang 0000-0003-1680-5957
Conceptualization (lead), Formal analysis (lead), Investigation (lead), Methodology (lead), Visualization (lead), Writing – original draft (lead), Writing – review & editing (lead)

Torge H Worbs 0009-0004-0187-6108
Formal analysis (supporting), Investigation (supporting), Visualization (supporting), Writing – review & editing (supporting)

Minhaj A Hussain 0000-0002-4833-7046
Investigation (supporting), Writing – review & editing (supporting)

Aman S Aberra 0000-0002-4805-541X
Investigation (supporting), Writing – review & editing (supporting)

Axel Thielscher 0000-0002-4752-5854
Conceptualization (supporting), Funding acquisition (supporting), Writing – review & editing (supporting)

Warren M Grill 0000-0001-5240-6588
Conceptualization (supporting), Funding acquisition (equal), Writing – review & editing (supporting)

Angel V Peterchev 0000-0002-4385-065X
Conceptualization (supporting), Funding acquisition (equal), Project administration (equal), Supervision (equal), Writing – review & editing (supporting)

Appendix

We derive the volume fraction formulas and the inverse relationships with the cell sizes for all neuron shapes, summarized in table A1. Formulas for simple geometries (parallel cylinders and hexagonal prisms in hexagonal grid, and spheres and truncated octahedrons in body-centered cubic lattice) are well known in literature and textbooks of various fields (mathematics, chemistry, crystallography, etc).

Parallel axons

In a 2D hexagonal grid, the unit cells are parallelograms with 60° and 120° angles (figure A1). With a side length d, the unit cells each have a cross-sectional area of $S_{UC} = \frac{\sqrt{3}}{2}d^2$ and contain a total intracellular volume equal to a full axon.

For circular axons with radius r, the cross-sectional areas are $S_{cir} = \pi r^2$. Therefore, the volume fraction is

$$f = \frac{S_{cir}}{S_{UC}} = \frac{2\pi r^2}{\sqrt{3}d^2},$$

and the radius can be given by the volume fraction as $r = \sqrt{\frac{\sqrt{3}f}{2\pi}}d$. The radius can be at most half the unit cell side length, i.e. $r \leq d/2$, at which point the membrane of neighboring axons come into contact and cut off current pathways through the extracellular space. The maximum volume fraction is therefore $f_{max} = \frac{\pi}{2\sqrt{3}} \approx 90.7\%$.

For axons with hexagonal cross sections of side length a, the cross-sectional areas are $S_{hex} = \frac{3\sqrt{3}}{2}a^2$. Therefore, the volume fraction is

$$f = \frac{S_{hex}}{S_{UC}} = \frac{3a^2}{d^2},$$

and the side length can be given by the volume fraction as $a = \sqrt{\frac{f}{3}}d \leq \frac{d}{\sqrt{3}}$, with the maximum side length achieved when the hexagons tile the 2D plane. Compared to cylindrical axons, the gaps between hexagonal axons have uniform width.

Cell bodies

In a body-centered cubic lattice with side length d, the unit cells each have a volume of $V_{UC} = d^3$ and contain a total volume equivalent to two full neurons (figure A2).

For spherical neurons with radius r, the volume of each neuron is $V_{Sph} = \frac{4\pi}{3}r^3$. Therefore, the volume fraction is

$$f = \frac{V_{Sph}}{V_{UC}} = \frac{8\pi r^3}{3d^3},$$

from which the inverse relationship is obtained as $r = \sqrt[3]{\frac{3f}{8\pi}}d$. The maximum volume fraction is reached when the neighboring neurons along the diagonal of the unit cells come into contact, and therefore $4r \leq \sqrt{3}d$, i.e. $r \leq \frac{\sqrt{3}}{4}d$, with $f_{max} = \frac{\pi\sqrt{3}}{8} \approx 68.0\%$. The space between neighboring neurons is not uniform and the minimal distance between diagonal neighbors, g_{diag}, is smaller than the axial neighbor distance, g_{axial}, by $\left(1 - \frac{\sqrt{3}}{2}\right)d$.

A truncated octahedron is formed from a regular octahedron (composed of eight equilateral triangles) by removing equilateral square pyramids with side length one third of the regular octahedron from its six vertices. With side length a, the volume of a truncated octahedron is $V_{TO} = 8\sqrt{2}a^3$. It can be calculated by obtaining the volume of a regular octahedron with side length $3a$, which is twice the volume of two equilateral square pyramids with the same length, $2 \cdot \frac{\sqrt{2}}{6}(3a)^3$. From this, the volumes of six equilateral square pyramids with side length a, $6 \cdot \frac{\sqrt{2}}{6}a^3$ is then subtracted. Therefore, the volume fraction is

$$f = \frac{2V_{TO}}{V_{UC}} = \frac{16\sqrt{2}a^3}{d^3},$$

and the inverse relationship is $a = \frac{\sqrt{2}\sqrt[3]{f}}{4}d \leq \frac{\sqrt{2}}{4}d$, with the maximum side length achieved when the octahedrons fill the space. Compared to spherical neurons, the gaps between pairs of opposing surfaces of neighboring truncated octahedral neurons have uniform widths within each face pair, with the gap widths between diagonal neighbors (hexagonal faces), g_{diag}, and axial neighbors (square faces), g_{axial}, having a constant ratio of $\frac{\sqrt{3}}{2}$.

Interleaved neurites

A 3D cross with circular cross section is formed from three cylinders with length d and radius r intersecting orthogonally at their mid-points (figure A3). The volume of each cylinder is $V_{cyl} = \pi r^2 d$, and the inclusion-exclusion formula is used to account for the intersecting region: $V_{Xcyl} = 3V_{cyl} - 3V_2 + V_3$,where $V_2 = \frac{16}{3}r^3$ and $V_3 = 8\left(2 - \sqrt{2}\right)r^3$ are the volumes of

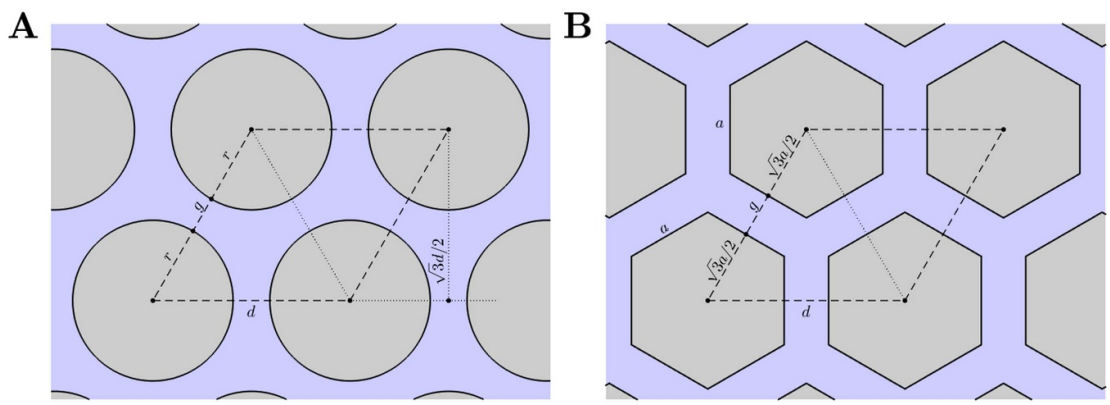

Figure A1. Hexagonal grids with cylindrical (A) and hexagonal (B) axons (gray), both at 60% volume fraction. Each unit cell (dashed lines) contains cross sections of four axons, adding up to a total of one axon.

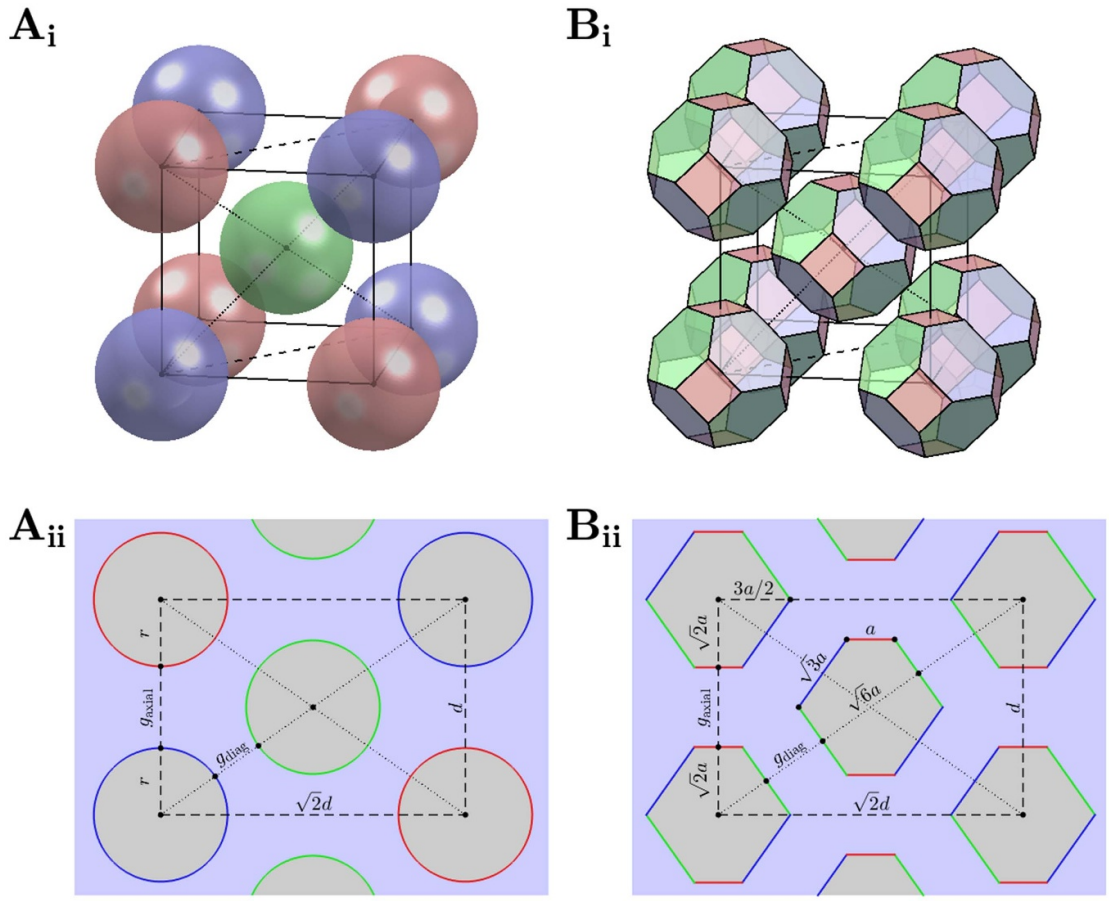

Figure A2. Body-centered cubic lattice with spherical (A) and truncated octahedral (B) neurons, both at low volume fraction of 25% for clarity. The upper panels show one unit cell (cube wire frame), which contains one full neuron at the center and eight one-eighth contributions from the corner neurons, for a total of two neurons. The lower panels show cross-sectional views through a diagonal plane (dashed line in upper panel) through the unit cells. Colors of neurons or surfaces are for illustration only.

a bicylinder (intersection of two cylinders) and a tri-cylinder (intersection of three cylinders), respectively. Therefore, the volume fraction is

$$f = \frac{2V_{\mathrm{Xcyl}}}{V_{\mathrm{UC}}} = \frac{6\pi r^2 d - 16\sqrt{2}r^3}{d^3}.$$

The maximum volume fraction is reached when neighboring neurons contact and therefore $4r \leq d$, i.e. $r \leq \frac{d}{4}$, with $f_{\max} = \frac{3\pi - 2\sqrt{2}}{8} \approx 82.5\%$.

The inverse relationship for the radius is obtained by solving the cubic equation

$$\alpha \hat{r}^3 + \beta \hat{r}^2 + f = 0$$

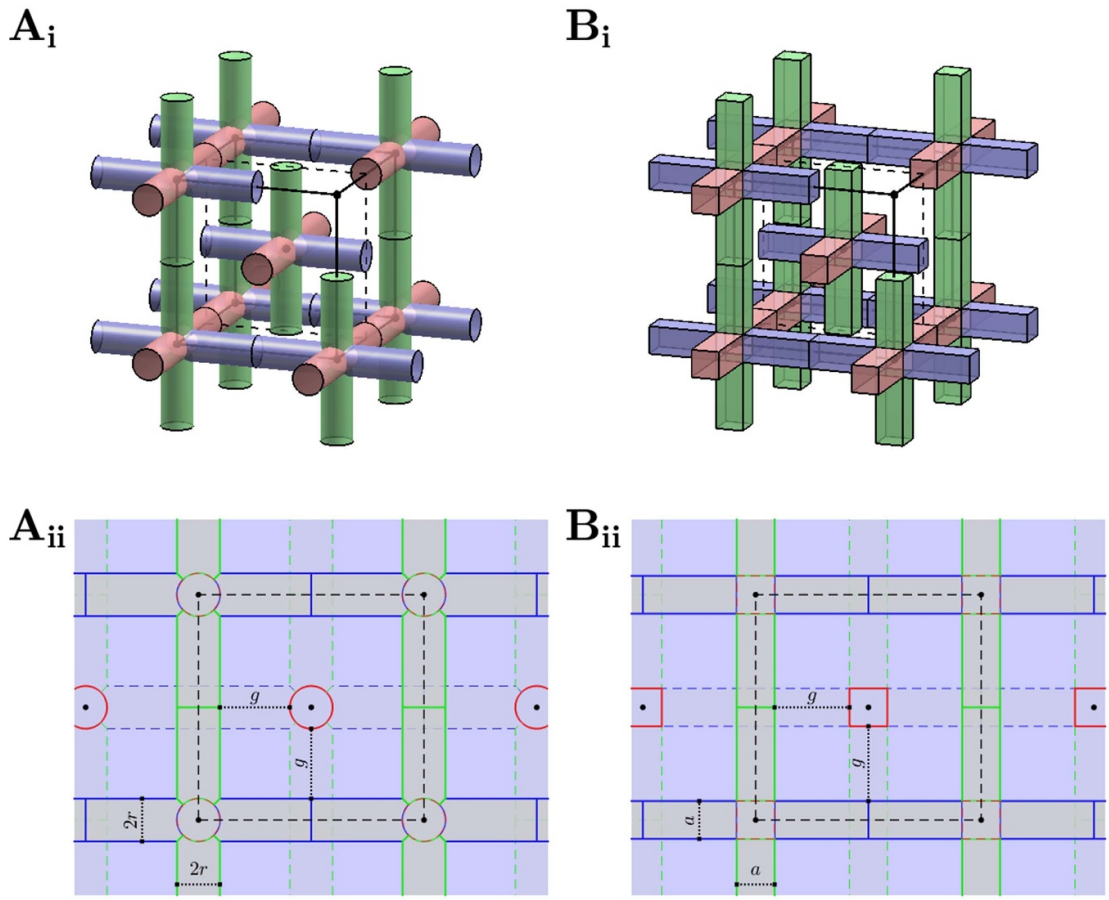

Figure A3. Body-centered cubic lattice of 3D-crosses with circular (A) and square (B) cross sections, both at low volume fraction of 15% and with one corner cell not shown for clarity. The lower panels show cross-sectional views of the front surface of the unit cells, with solid lines indicating cell membranes in the surface plane, while dashed lines indicate membranes from the mid-plane of the unit cell (dashed line in upper panels) projected onto the same view. The gap size is indicated for neurons neighboring in the diagonal direction, as neurons neighboring in the axial direction are always in direct contact. Colors of neurons or surfaces are for illustration only.

with $\hat{r} = r/d$ and coefficients $\alpha = 16\sqrt{2}$ and $\beta = -6\pi$ corresponding to the cubic and quadratic terms, respectively. The discriminant $\Delta = \left(4|\beta|^3 - 27\alpha^2 f\right) \cdot f = \left(864\pi^3 - 13824 \cdot f\right) \cdot f \geq 0$ for all $f \in [0, f_{\max}]$, and therefore the cubic equation has three real roots—distinct non-zero roots for $f \neq 0$ or a double root of 0 for $f = 0$. The roots can be expressed using trigonometric functions as

$$\hat{r} = 2\sqrt{-\frac{p}{3}}\cos\left[\frac{1}{3}\mathrm{acos}\left(\frac{3q}{2p}\sqrt{-\frac{3}{p}}\right) - \frac{2\pi}{3}k\right] - \frac{\beta}{3\alpha},$$

$k = 0, 1, 2,$

where $p = -\frac{\beta^2}{3\alpha^2}$, $q = -\frac{\beta^2}{27\alpha^2} + \frac{f}{\alpha}$, and $k = 1$ for $\hat{r} \in \left[0, \frac{1}{4}\right]$. (The other two solutions with $k = 0$ and $k = 2$ correspond to roots $\hat{r} \geq \frac{|\beta|}{\alpha} \approx 0.83$ and $\hat{r} \leq 0$, respectively.) This expression can be simplified as

$$\hat{r} = \frac{2|\beta|}{3\alpha}\left\{\cos\left[\frac{1}{3}\mathrm{acos}\left(1 - \frac{27\alpha^2 f}{2|\beta|^3}\right) - \frac{2\pi}{3}\right] + \frac{1}{2}\right\},$$

and therefore

$$r = \frac{\pi\sqrt{2}}{8}\left\{\cos\left[\frac{1}{3}\mathrm{acos}\left(1 - \frac{32f}{\pi^3}\right) - \frac{2\pi}{3}\right] + \frac{1}{2}\right\} \cdot d.$$

A 3D cross with square cross section is formed from three square rectangular prisms with length d and side length a intersecting orthogonally at their mid-points. The volume of 3D cross is $V_{\mathrm{Xsq}} = 3(d-a)a^2 + a^3$ and the volume fraction is

$$f = \frac{2V_{\mathrm{Xsq}}}{V_{\mathrm{UC}}} = \frac{6a^2 d - 4a^3}{d^3}.$$

The condition of contact between neurons neighboring in the diagonal direction is $2a \leq d$, i.e. $a \leq \frac{d}{2}$. With $\alpha = 4$, and $\beta = -6$ for the corresponding cubic equation, the inverse relationship for the side length can be similarly obtained as

$$a = \left\{\cos\left[\frac{\mathrm{acos}(1-f) - 2\pi}{3}\right] + \frac{1}{2}\right\} \cdot d.$$

Table A1. Models and parameters for representing different neural tissue types.

Tissue type (model dimension)	Lattice with unit cell of side length d and orientations explored	Shape of cells or their cross sections with side length $\hat{a}$ or radius $\hat{r}$ and their maximum (normalized to)		Volume fraction f and its limits (if less than 100%)	Inverse relationship of volume fraction and neuron size	Size of gap[a] $\hat{g}$ between cells (normalized to d)
Parallel fibers (2D, transverse)	Hexagon grid, 0° to 30°, in steps of 5°	Circle	$\hat{r} \leq \frac{1}{2}$	$f = \frac{2\pi}{\sqrt{3}} \cdot \hat{r}^2 \leq \frac{\pi}{2\sqrt{3}}$	$\hat{r} = \sqrt[4]{3}\sqrt{\frac{f}{2\pi}}$	$\hat{g} = 1 - 2\hat{r}$
		Hexagon	$\hat{a} \leq \frac{1}{\sqrt{3}}$	$f = 3 \cdot \hat{a}^2$	$\hat{a} = \sqrt{\frac{f}{3}}$	$\hat{g} = 1 - \sqrt{3}\hat{a}$
Cell bodies (3D)	Body-centered cubic lattice, Miller-indices [100], [110], [111]	Sphere	$\hat{r} \leq \frac{\sqrt{3}}{4}$	$f = \frac{8\pi}{3} \cdot \hat{r}^3 \leq \frac{\sqrt{3}\pi}{8}$	$\hat{r} = \sqrt[3]{\frac{3f}{8\pi}}$	$\hat{g}_{\text{diag}} = \frac{\sqrt{3}}{2} - 2\hat{r}$ $\hat{g}_{\text{axial}} = 1 - 2\hat{r}$
		Truncated octahedron	$\hat{a} \leqslant \frac{1}{2\sqrt{2}}$	$f = 16\sqrt{2} \cdot \hat{a}^3$	$\hat{a} = \frac{\sqrt{2}\sqrt[3]{f}}{4}$	$\hat{g}_{\text{diag}} = \frac{\sqrt{3}}{2} - \sqrt{6}\hat{a}$ $\hat{g}_{\text{axial}} = 1 - 2\sqrt{2}\hat{a}$
Dense interleaved neurites (3D)		3D cross with length d and circular cross section	$\hat{r} \leq \frac{1}{4}$	$f = \left(6\pi - 16\sqrt{2}\hat{r}\right) \cdot \hat{r}^2 \leq \frac{3\pi - 2\sqrt{2}}{8}$	$\hat{r} = \frac{\pi\sqrt{2}}{8}\left\{\cos\left[\frac{1}{3}\text{acos}\left(1 - \frac{32f}{\pi^3}\right) - \frac{2\pi}{3}\right] + \frac{1}{2}\right\}$	$\hat{g} = 1 - 4\hat{r}$
		3D cross with length d and square cross section	$\hat{a} \leq \frac{1}{2}$	$f = 2\left(3 - 2\hat{a}\right) \cdot \hat{a}^2$	$\hat{a} = \cos\left[\frac{\text{acos}(1-f) - 2\pi}{3}\right] + \frac{1}{2}$	$\hat{g} = 1 - 2\hat{a}$

[a] Gap sizes refer to minimum surface-to-surface distances between neighboring neurons. For 3D crosses, gap size is for neighboring neurons in the diagonal direction, as neighboring neurons in the axial direction are in direct contact.

Table A2. COMSOL mesh setting for general physics.

Model	Mesh setting	Minimum element size (nm)	Maximum element size (μm)	Maximum growth factor	Curvature factor
2D	Finer	22.7	6.73	1.25	0.25
	Extra fine	13.6	3.64	1.2	0.25
3D	Fine	606	4.85	1.45	0.5
	Finer	242	3.33	1.4	0.4

References

[1] Peterchev A V, Wagner T A, Miranda P C, Nitsche M A, Paulus W, Lisanby S H, Pascual-Leone A and Bikson M 2012 Fundamentals of transcranial electric and magnetic stimulation dose: definition, selection, and reporting practices *Brain Stimul.* **5** 435–53

[2] Aberra A S, Wang B, Grill W M and Peterchev A V 2020 Simulation of transcranial magnetic stimulation in head model with morphologically-realistic cortical neurons *Brain Stimul.* **13** 175–89

[3] Koponen L M, Nieminen J O, Mutanen T P, Stenroos M and Ilmoniemi R J 2017 Coil optimisation for transcranial magnetic stimulation in realistic head geometry *Brain Stimul.* **10** 795–805

[4] Wang B and Aberra A S 2025 Bridging macroscopic and microscopic modeling of electric field by brain stimulation *Brain Stimul.* **18** 897–9

[5] Agudelo-Toro A and Neef A 2013 Computationally efficient simulation of electrical activity at cell membranes interacting with self-generated and externally imposed electric fields *J. Neural Eng.* **10** 026019

[6] Qi Z *et al* 2025 Enabling electric field model of microscopically realistic brain *Brain Stimul.* **18** 77–93

[7] Weise K, Makaroff S N, Numssen O, Bikson M and Knösche T R 2025 Statistical method accounts for microscopic electric field distortions around neurons when simulating activation thresholds *Brain Stimul.* **18** 280–6

[8] Qi Z *et al* 2025 Importance of considering microscopic structures in modeling brain stimulation *Brain Stimul.* **18** 1150–2

[9] Weise K *et al* 2025 Microscopic electric fields form mesoscale electric fields and influence TMS activation thresholds *Brain Stimul.* **18** 1852–4

[10] Wang B, Hussain M A, Worbs T, Thielscher A, Grill W M and Peterchev A V 2025 Single pointwise samples of electric field on a neuron model cannot predict activation threshold by brain stimulation *Brain Stimul.* **18** 1667–70

[11] Yedlin M, Kwan H, Murphy J T, Nguyen-Huu H and Wong Y C 1974 Electrical conductivity in cat cerebellar cortex *Exp. Neurol.* **43** 555–69

[12] Hoeltzell P B and Dykes R W 1979 Conductivity in the somatosensory cortex of the cat—evidence for cortical anisotropy *Brain Res.* **177** 61–82

[13] Holsheimer J 1987 Electrical conductivity of the hippocampal CA1 layers and application to current-source-density analysis *Exp. Brain Res.* **67** 402–10

[14] Goto T, Hatanaka R, Ogawa T, Sumiyoshi A, Riera J and Kawashima R 2010 An evaluation of the conductivity profile in the somatosensory barrel cortex of Wistar rats *J. Neurophysiol.* **104** 3388–412

[15] Lee S, Falchier A and Opitz A 2026 Layer-specific electric fields and effective conductivity in nonhuman primates during transcranial electrical stimulation *Brain Stimul.* **19** 103060

[16] Karwoski C J, Frambach D A and Proenza L M 1985 Laminar profile of resistivity in frog retina *J. Neurophysiol.* **54** 1607–19

[17] Wang B and Weiland J D 2015 Resistivity profiles of wild-type, rd1, and rd10 mouse retina. *2015 37th Annu. Int. Conf. IEEE Eng. Med. Biol. Soc. EMBC* (*Milan, Italy*) pp 1650–3

[18] Kasi H, Meissner R, Babalian A, van Lintel H, Bertsch A and Renaud P 2011 Direct localised measurement of electrical resistivity profile in rat and embryonic chick retinas using a microprobe *J. Electr. Bioimpedance* **1** 84–92

[19] Manola L, Roelofsen B H, Holsheimer J, Marani E and Geelen J 2005 Modelling motor cortex stimulation for chronic pain control: electrical potential field, activating functions and responses of simple nerve fibre models *Med. Biol. Eng. Comput.* **43** 335–43

[20] Loizos K, RamRakhyani A K, Anderson J, Marc R and Lazzi G 2016 On the computation of a retina resistivity profile for applications in multi-scale modeling of electrical stimulation and absorption *Phys. Med. Biol.* **61** 4491–505

[21] Mosayebi-Samani M, Cunha T, Eroğlu H H, Siebner H R, Nitsche M A and Thielscher A 2025 The effect of brain tissue anisotropy on the electric field caused by transcranial electric stimulation: sensitivity analysis and magnetic resonance electrical impedance tomography *Imaging Neurosci.* **3** imag_a_00481

[22] Katoch N, Choi B-K, Park J-A, Ko I-O and Kim H-J 2021 Comparison of five conductivity tensor models and image reconstruction methods using MRI *Molecules* **26** 5499

[23] Lee S, Zhao Z, Alekseichuk I, Park J, Shirinpour S, Linn G, Schroeder C E, Falchier A Y and Opitz A 2025 Layers of the monkey visual cortex are selectively modulated during electrical stimulation *PLoS Biol.* **23** e3003278

[24] Wang B, Peterchev A V, Gaugain G, Ilmoniemi R J, Grill W M, Bikson M and Nikolayev D 2024 Quasistatic approximation in neuromodulation *J. Neural Eng.* **21** 041002

[25] Kjer H M *et al* 2025 Bridging the 3D geometrical organisation of white matter pathways across anatomical length scales and species *eLife* **13** RP94917

[26] Shapson-Coe A *et al* 2024 A petavoxel fragment of human cerebral cortex reconstructed at nanoscale resolution *Science* **384** eadk4858

[27] Adler A and Boyle A 2017 Electrical impedance tomography: tissue properties to image measures *IEEE Trans. Biomed. Eng.* **64** 2494–504

[28] Linderholm P, Marescot L, Loke M H and Renaud P 2008 Cell culture imaging using microimpedance tomography *IEEE Trans. Biomed. Eng.* **55** 138–46

[29] Logothetis N K, Kayser C and Oeltermann A 2007 *In vivo* measurement of cortical impedance spectrum in monkeys: implications for signal propagation *Neuron* **55** 809–23

[30] Nicholson P W 1965 Specific impedance of cerebral white matter *Exp. Neurol.* **13** 386–401

[31] Korogod N, Petersen C C and Knott G W 2015 Ultrastructural analysis of adult mouse neocortex comparing aldehyde perfusion with cryo fixation *eLife* **4** e05793

[32] Turner N L *et al* 2022 Reconstruction of neocortex: organelles, compartments, cells, circuits, and activity *Cell* **185** 1082–1100.e24

[33] MICrONS Consortium MICrONS explorer layer 2/3 2026 (available at: www.microns-explorer.org/phase1).

[34] Pelot N A, Behrend C E and Grill W M 2019 On the parameters used in finite element modeling of compound peripheral nerves *J. Neural Eng.* **16** 016007
[35] Monfared O, Tahayori B, Freestone D, Nešić D, Grayden D B and Meffin H 2020 Determination of the electrical impedance of neural tissue from its microscopic cellular constituents *J. Neural Eng.* **17** 016037
[36] Lehmenkühler A, Syková E, Svoboda J, Zilles K and Nicholson C 1993 Extracellular space parameters in the rat neocortex and subcortical white matter during postnatal development determined by diffusion analysis *Neuroscience* **55** 339–51
[37] Noetscher G *et al* 2026 Direct reconstruction of DC cortical conductivity from large-scale electron microscopy data *bioRxiv* (https://doi.org/10.64898/2026.03.23.713806)
[38] Tamada H, Blanc J, Korogod N, Petersen C C and Knott G W 2020 Ultrastructural comparison of dendritic spine morphology preserved with cryo and chemical fixation *eLife* **9** e56384
[39] Griswold J M *et al* 2024 Membrane mechanics dictate axonal pearls-on-a-string morphology and function *Nat. Neurosci.* **28** 1–13
[40] Nicholson C and Hrabětová S 2017 Brain extracellular space: the final frontier of neuroscience *Biophys. J.* **113** 2133–42
[41] Velicky P *et al* 2023 Dense 4D nanoscale reconstruction of living brain tissue *Nat. Methods* **20** 1256–65
[42] Maxwell J C 1873 *A Treatise on Electricity and Magnetism* vol 1 (Clarendon press)
[43] Rayleigh L 1892 On the influence of obstacles arranged in rectangular order upon the properties of a medium *Lond. Edinb. Dublin Philos. Mag. J. Sci.* **34** 481–502
[44] Runge V I 1925 Zur elektrischen Leitfähigkeit metallischer Aggregate *Z. Tech. Phys.* **6** 61–68
[45] Meredith R E and Tobias C W 1960 Resistance to potential flow through a cubical array of spheres *J. Appl. Phys.* **31** 1270–3
[46] Peters M J, Stinstra G and Hendriks M 2001 Estimation of the electrical conductivity of human tissue *Electromagnetics* **21** 545–57
[47] Pavlin M and Miklavcic D 2009 The effective conductivity and the induced transmembrane potential in dense cell system exposed to DC and AC electric fields *IEEE Trans. Plasma Sci.* **37** 99–106
[48] Pelot N A, Thio B J and Grill W M 2018 Modeling current sources for neural stimulation in COMSOL *Front. Comput. Neurosci.* **12** 40
[49] Roth B J, Gielen F L H and Wikswo J P 1988 Spatial and temporal frequency-dependent conductivities in volume-conduction calculations for skeletal muscle *Math. Biosci.* **88** 159–89
[50] Meffin H, Tahayori B, Sergeev E N, Mareels I M Y, Grayden D B and Burkitt A N 2014 Modelling extracellular electrical stimulation: III. Derivation and interpretation of neural tissue equations *J. Neural Eng.* **11** 065004
[51] Tao L and Nicholson C 2004 Maximum geometrical hindrance to diffusion in brain extracellular space surrounding uniformly spaced convex cells *J. Theor. Biol.* **229** 59–68
[52] Krassowska W and Neu J C 1994 Response of a single cell to an external electric field *Biophys. J.* **66** 1768–76
[53] Wang B, Aberra A S, Grill W M and Peterchev A V 2018 Modified cable equation incorporating transverse polarization of neuronal membranes for accurate coupling of electric fields *J. Neural Eng.* **15** 026003
[54] Baumann S B, Wozny D R, Kelly S K and Meno F M 1997 The electrical conductivity of human cerebrospinal fluid at body temperature *IEEE Trans. Biomed. Eng.* **44** 220–3
[55] Østby I *et al* 2009 Astrocytic mechanisms explaining neural-activity-induced shrinkage of extraneuronal space *PLoS Comput. Biol.* **5** e1000272
[56] Florence C M, Baillie L D, Mulligan S J and Mongin A A 2012 Dynamic volume changes in astrocytes are an intrinsic phenomenon mediated by bicarbonate ion flux *PLoS One* **7** e51124
[57] Walch E and Fiacco T A 2022 Honey, I shrunk the extracellular space: measurements and mechanisms of astrocyte swelling *Glia* **70** 2013–31
[58] Xie L *et al* 2013 Sleep drives metabolite clearance from the adult brain *Science* **342** 373–7
[59] Gabriel C, Peyman A and Grant E H 2009 Electrical conductivity of tissue at frequencies below 1 MHz *Phys. Med. Biol.* **54** 4863
[60] Tao A, Tao L and Nicholson C 2005 Cell cavities increase tortuosity in brain extracellular space *J. Theor. Biol.* **234** 525–36
[61] Joucla S and Yvert B 2009 The "mirror" estimate: an intuitive predictor of membrane polarization during extracellular stimulation *Biophys. J.* **96** 3495–508
[62] Wang B, Grill W M and Peterchev A V 2025 Cell volume fraction determines layer-specific tissue conductivity in the cortex *Neural Interfaces 2025* (Arlington, VA, USA, *VA, USA*, June 2025)